An Efficient Simulation of Skin Contact Deformation for Virtual Ergonomic Assessments of Handheld Products

Yulai Xie*, Satoshi Kanai, and Hiroaki Date

Graduate School of Information Science and Technology, Hokkaido University, Sapporo, Japan

Abstract – **Skin contact conditions play a significant role in the virtual ergonomic assessment of handheld products. In this paper, in order to simulate the skin contact deformation mechanism, a physical model based on the Boussinesq approximation with nonlinear elasticity and a compressing-swelling effect was proposed. The parameters of this model were estimated by fitting experimental data. Based on the model, a skin deformation simulation, including a pre-process and an online process, was presented. The spatially distributed heterogeneity of the skin was realized by partitioning the hand surface according to anatomical knowledge. The contact situations were simulated in the simple case of finger and palm deformation and complex grasp posture. The estimated contact conditions, such as contact pressure distribution, were compared with measurements. The results indicated that this method had a higher efficiency, validity, and extensibility.**

Keywords: **efficient simulation, skin contact deformation, virtual ergonomic assessment**

1. Introduction

Handheld products, such as portable digital appliances, have been widely used in daily life and production activities. For their customers, an ergonomic design is always desired for better user experience and high productivity. Therefore, during the development process of handheld products, many grasp factors need to be assessed, for instance, grasp stability, grasp comfort, and grasp safety.

3D human hand modeling and simulation, such as [1] and [2-4], provides significant advantages for ergonomic assessments when incorporated into the early stage of the design process of handheld products. They can, especially, reduce the need for sensory tests on human subjects and also for expensive prototypes, thus reducing costs and time to market. However, one challenge is mimicking the skin deformation caused by physical contact with a product surface.

The biomechanical property of human skin plays a fundamental role in the tactile sense of humans [5,6]. Its structure and the material behavior exhibit extreme complexities: layered structure, nonlinear elasticity, near incompressibility, spatially distributed heterogeneity, etc. [7]. The skin contact conditions, such as contact force, contact area, and contact pressure distribution, between the grasping hand and the grasped objects directly affect grasp factors including grasp stability, comfort, safety, etc. Hence the contact conditions always serve as impor-

tant indicators for ergonomic assessments of handheld products.

Many studies [8-15] have reported that the contact conditions of grasp postures are used in the grasp factors evaluation. Although, it is still difficult to deal with complex contact configurations where the products have irregular and curved geometrical shapes, due to the limitation of the resolution or shape of sensors.

Our research group [2-4,16] has been proposing the *Digital Hand* which is a 3D virtual hand model and a virtual ergonomic assessment system for handheld products. As shown in Fig. 1(a) and (b), the Digital Hand is composed of a surface skin model represented by a triangular mesh and an internal skeletal structure model. The geometries of its surface skin and the inner bones are derived from MRI measurements of different grasp postures of a specific subject. Moreover, it can generate plausible grasp postures shown in Fig. 1(c) by optimization techniques, and quantitatively estimate the grasp stability and the ease of grasp in different grasp postures.

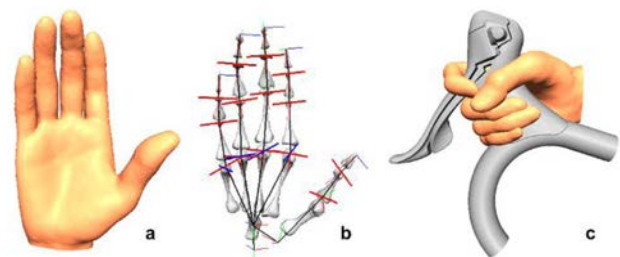However, the Digital Hand has not simulated skin con-

*Corresponding author: Yulai Xie
 Tel: +81-11-706-6449
 Fax: +81-11-706-7126
 E-mail: y_xie@sdm.ssi.ist.hokudai.ac.jp

Fig. 1. Digital Hand: (a) surface skin model, (b) internal skeletal structure model, (c) generated grasp posture.

tact deformation, and instead approximated it in a simple way where the interpenetration within a specific threshold was allowed between the skin and the surfaces. Accordingly, the contact force can not be estimated at all, which was against the valid and precise evaluation of the grasp stability. In addition, the ease of grasp was still estimated based on the subjective evaluations. However, an objective evaluation is desired for excluding personal preferences.

The objective of this paper is to propose an efficient method to simulate the contact deformation of human hand skin for satisfying the requirements of virtual ergonomic assessment of handheld products in the Digital Hand: sufficient accuracy, efficiency, and extensibility in a complex contact configuration with product surfaces. First, a physical model of the deformation based on the Boussinesq approximation is introduced in the simulation. In this model, nonlinear elasticity and a compressing-swelling effect on human skin are modeled. Moreover, the palmar surface is partitioned into different regions for consideration of the spatially distributed heterogeneity of the human hand. The parameters needed in the physical model are estimated by fitting the empirical data. Finally, based on the physical model, an online process based on a quasi-rigid object approximation realizes the efficient simulation of the skin contact deformation.

The effectiveness and accuracy of our proposed simulation method are demonstrated for simple fingertip as well as palm skin deformations and for complex contact configurations, grasping cylinders or other handheld products where the basic grasp posture of the human hand model for the skin contact deformation is given by the Digital Hand.

2. Related Work on the Skin Contact Deformation Simulation

As for the skin contact deformation simulation, the studies have been done in many fields; robotics, biomechanics, computer graphics, etc.. However, the simulation methods are basically classified into FEM-based methods and other physics-based methods.

2.1. FEM-based methods

Finite element analysis is commonly preferred for the accurate simulation of skin deformation [5,15,17,18]. Some studies based on the FEM can estimate the pressure distribution of grasping hand [19] and foot [20]. Despite its high accuracy involving the large computation time, FEM obviously is not appropriate for a practical virtual ergonomic assessment system for handheld products. This is because in such system, a large number of grasp postures with different hand sizes need to be evaluated within an acceptable period of design, and therefore the simulation of skin contact deformation for one posture needs to finish as quickly as possible.

2.2. Other physics-based methods

Different from the FEM-based methods, the simulation in computer graphics aims for approximate but efficient contact deformation between general objects. The work [21] efficiently simulates the contact deformation and estimates surface pressure distribution. The Boussinesq approximation, which is a linear constitutive model, is adopted as the basic physical model for their work. Also, their technique treats the deformable model as a "quasi-rigid" object for efficient online process of the simulation.

Our proposed approach shares the strategy of Pauly's work [21], but, unlike theirs, the physical model is extended to realize the nonlinear elasticity of human hand skin. Moreover, their work assumes objects are homogeneous. However, our study treats the human hand as a heterogeneous material which has spatially varying material parameters, such as Young's modulus.

[22] realizes a physics-based deformation simulation of soft contact where the human skeleton is comprised of articulated bones, each of which is surrounded by a set of mass points representing the deformable skin surface. The deformation is also confined to a subset of the vertices around the contact site.

However, these two studies in computer graphics mainly aim to realize visually realistic deformations. They choose the material parameters arbitrarily which do not resemble human skin in the real world. In addition, their studies are lack of experimental validations.

3. Methods

The simulation method is composed of two main parts: 1) a physical model of the deformation, and 2) a deformation simulation algorithm.

In the first part, a linear physical model of skin contact deformation, called Boussinesq approximation, is adopted and is extended with nonlinear elasticity and a compressing-swelling effect in order to mimic realistic deformation of human hand skin. The material parameters of this effect were determined by the experimental data (Section 3.1.5).

In the second part as shown in Fig. 2, based on the proposed physical model, an algorithm including a preprocess and an online process in order to simulate skin deformation is developed. In the pre-process, the surface skin model is partitioned into 19 sub-surfaces according to hand surface anatomical knowledge (A1). Then, the point-force-based discretization of the physical model in each sub-surface is executed (A2). For one Digital Hand model, the pre-process has to be executed only once. In the online process, first of all, a collision detection algorithm is done to find collision regions (A3), and they are locally enlarged to get an active region (A4). After that, the active region is separated into sub-active regions (A5). For each sub-active region, a response matrix is composed and a sub-matrix is extracted from
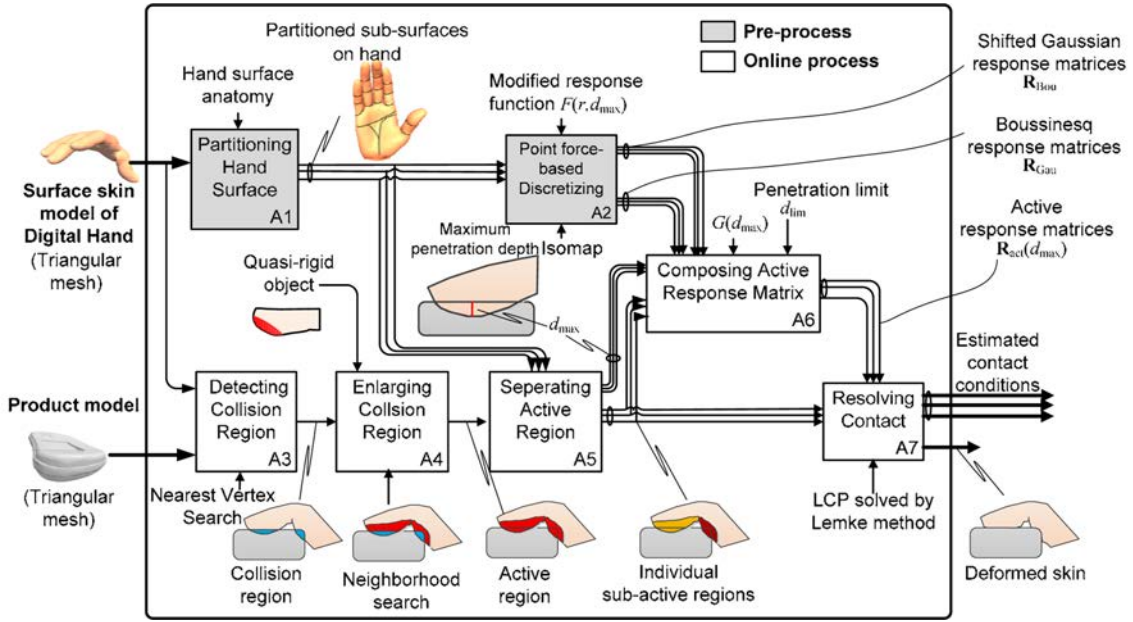
Fig. 2. Our proposed simulation method of skin contact deformation. Three arrow lines with a circle mean multiple components in the pipeline. For example, in A1, the surface skin model is partitioned into multiple sub-surfaces.

it (A6). Finally, the contact deformations over the sub-active regions are simulated by solving the Linear Complementarity Problem (LCP) (A7). The relation between the shear modulus and the maximum penetration depth is tuned until the output best fits the experimental data. The details of the processes are described in the following sections.

3.1. Physical model of skin contact deformation
3.1.1. Boussinesq approximation

Boussinesq approximation, a widely used method in contact mechanics, models linear elasticity with a constant shear modulus in small deformation. It approximates the surface deformation around a contact point within an elastic half space [23]. As shown in Fig. 3, when a normal compressive force with a magnitude p acts at the origin of a plane, the displacement $u(r)$ at any position is expressed by Eq. 1:

Fig. 3. Response function of the Boussinesq approximation.

$$u(r) = \frac{(1-\upsilon)p}{2\pi Gr} = f(r)p \tag{1}$$

$$f(r) = \begin{cases} \dfrac{(1-\upsilon)p}{2\pi Gr} & (r \geq r_0) \\[2ex] \dfrac{(1-\upsilon)p}{2\pi Gr_0} & (r < r_0) \end{cases} \tag{2}$$

where, r is the distance between an arbitrary point and the origin, $u(r)$ the displacement at the point due to a force p, u Possion's ratio, G shear modulus, $f(r)$ defined by Eq. 2 is called a *response function* as shown in Fig. 3. In order to avoid the singularity problem of $f(r)$ when $r = 0$, there is a special treatment. If $r < r_0$, where $r_0 = 0.5$ mm, then $f(r) = f(r_0)$.

3.1.2 Nonlinear elasticity of skin

Human skin has a complicated biological structure and presents nonlinear elasticity in the stress-strain relation [5,6,24]. For ergonomic assessments of the handheld products, the external geometry of hands is mainly considered, and therefore hand skin could be treated as a bulk material [25]. This means that the layered structure of skin is ignored, and the physical property presented by external skin is used to represent that of the entire skin structure. In most indentation studies on skin and subcutaneous tissue, researchers have assigned Possion's ratio u within a range of 0.45 to 0.5 in order to simulate the nearly incompressible behavior of the soft tissue [26, 27]. Similar to them, and to our proposed physical model simplistic, u was fixed at 0.5.

Dandekar et al. [5] indicate that G of the human hand skin ranges from 0.004 Mpa to 0.08 Mpa depending on
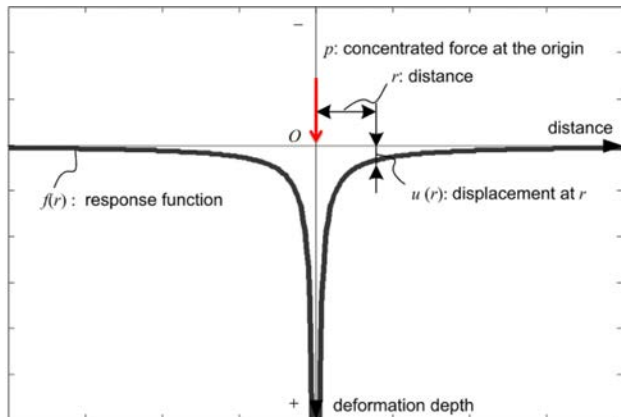
the nonlinear elasticity. This range is referred to for our proposed physical model. However, choosing the right material parameters of the model is still a difficult and time-consuming process. When involving nonlinearity, the process becomes more challenging. Hence, the shear modulus G was tuned until it best fits the empirical data (Section 4.1), similar to the other measurement-based models [28,29].

3.1.3 Compressing-swelling effect

As human skin is a nearly incompressible material [25], in the skin deformation simulation of our study, the *compressing-swelling effect* on human skin needs to be realized. It means that a compressive force causes not only volume compression in the region to which the force is applied (force-applied region), but also volume swelling right outside the region due to the near volume preserving property. However, as shown in Fig. 4, the volume after deformation is obviously reduced when only using the original Boussinesq approximation, and this leads to physically behave as a sponge-like material. The compressing-swelling effect of an incompressible material, such as a soft tissue, is shown in Fig. 4(c). In the hand skin simulation, the effect was realized by modifying the original Boussinesq approximation which was described in Section 3.1.5, for producing a more realistic visual deformation.

3.1.4 Modified physical model with nonlinear elasticity

For realizing nonlinear elasticity in the physical model, shear modulus G is regarded as a linear function of the maximum penetration depth, d_{max}, among the vertices in the force-applied region as Eq. 3:

$$G(d_{max})=G_0+(G_{lim}-G_0)\frac{d_{max}}{d_{lim}} \quad (0 \leq d_{max} \leq d_{lim}) \quad (3)$$

where G_0 is an initial shear modulus, G_{lim} a limit shear modulus, and d_{lim} a limit penetration depth.

From the experiments of Section 4.1, the actual value of d_{lim} was measured for simple fingertip and palm deformation. Moreover, G_0 and G_{lim} were chosen by fitting

the empirical data of the maximum penetration depth versus the contact force. Therefore, by substituting Eq. 3 into Eq. 1, the response function $f(r)$ of the linear case in Eq. 1 is rewritten into the nonlinear case as Eq. 4. To keep it simple, $f(r)$ is still used to express Eq. 4 in Section 3.1.5.

$$f(r,d_{max})=\frac{1}{4\pi G(d_{max})r} \quad (4)$$

3.1.5 The compressing-swelling effect and indentation test

Moreover, to realize the compressing-swelling effect in the Boussinesq approximation, as shown in Fig. 5, we modulated the original Boussinesq approximation (the dashed curve), by adding a shifted negative Gaussian function (the red curve). As a result, the modified response function (the thick blue curve) $F(r)$ can be obtained as Eq. 5:

$$F(r)=f(r)+\{-g(r)\}=f(r)+\left\{-ae^{\frac{-(r-b)^2}{2c^2}}\right\} \quad (5)$$

where $g(r)$ is the shifted Gaussian function.

Indentation tests were conducted both on finger and palm skin, in order to find the proper parameter setting of a, b, and c of $g(r)$ in Eq. 5. Fig. 6(a), (b), and Table 1 shows the experimental setting. The 3D point clouds obtained by the 3D laser scanner were evaluated as shown in Fig. 6(c). The final setting of $g(r)$ is listed in Table 2, when 1 N was applied to the indentor whose diameter was 2 mm.

Moreover, physical properties of swelling bulges of skin were also tested. It was found that the change of a swelling bulge was very small when the compressing force varied, because the change of skin volume rapidly approximated a limit caused by the nonlinear elasticity of skin. As shown in Fig. 7(b), the change of the height of the bulge between the red bulge (generated by an indentor) and the dashed bulge (generated by the indentor
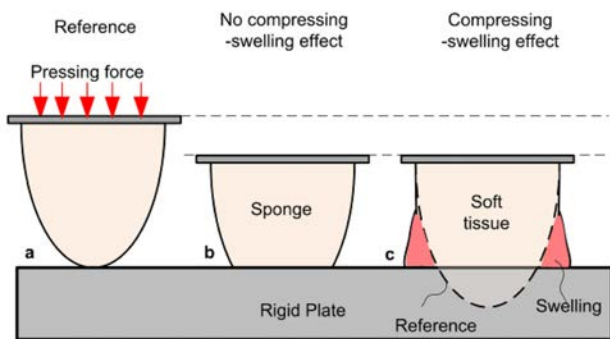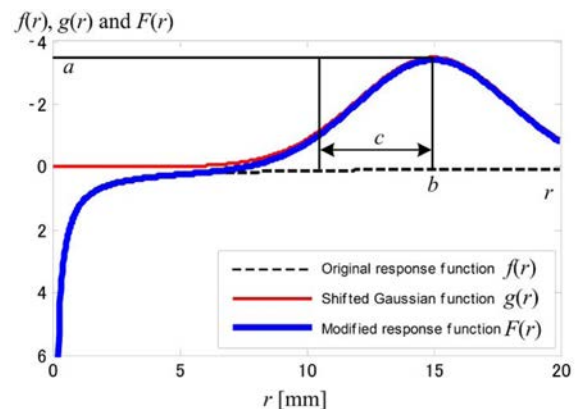

Fig. 4. Compressing-swelling effect: (a) reference, (b) compressible sponge (without compressing-swelling effect), (c) incompressible soft tissue (with compressing-swelling effect).

Fig. 5. Our modified response function.

Fig. 6. Indentation test: (a) experimental setting, (b) real scene, and (c) a cross section of 3D deformation map (Geomagic).

Table 1. The setting of indentation test

Subjects (fingertip deformation)	3 males, 23-27 years, right hand
Force gauge (IMADA DPS-20R)	Measuring the indentation force
3D laser scanner (Konica Minolta Vivid 910)	Taking 3D point clouds on skin shapes before and after indentations
Fixture (a hard foam material)	Supporting and fixing the palm

Table 2. Setting of *a*, *b* and *c*

	Palm [mm] (average)	Finger [mm] (average)
a	3	2
b	15	8
c	2.5	2

in Fig. 7(a)) was 0.1 mm which could be neglected. Therefore, *a* in Eq. 5 is regarded as a function of the maximum penetration depth d_{max} as Eq. 6, which ensures different contact forces resulting in a constant height of a swelling bulge:

$$a(d_{max}) = a_0 \frac{G_0}{G(d_{max})} \qquad (6)$$

where a_0 is an initial height of the shifted Gaussian function which is the height when 1 N was applied to the indentor.

In addition, as shown in Fig. 8, an obvious bulge, which was formed by the root of the fingers caused by the finger bending, was pushed by the indentor. The swelling bulge exhibits extreme softness. They could be easily flattened almost effortlessly, differing from the case of the indentation test of Fig. 7(b). Therefore, as shown in Fig. 7(c), if the bulges (dashed one generated by the reference indentor) appear in a force-applied region, they will be ignored, as Eq. 7, instead of Eq. 6. Only the swe-
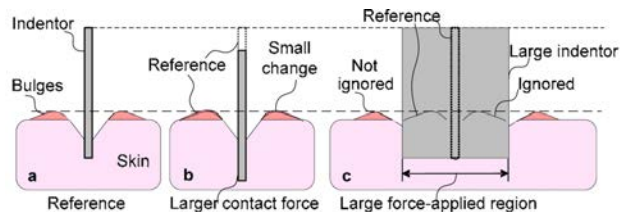
lling bulges (red ones) right outside the region needed to be simulated for visualization purposes.

$$a(d_{max}) = 0 \qquad (7)$$

By introducing this dependency of *a* with d_{max}, the modified response function in Eq. 5 becomes Eq. 8. To keep it simple, $F(r)$ was still used to express Eq. 8.

$$F(r, d_{max}) = f(r, G(d_{max})) + \left\{ -a(d_{max}) e^{\frac{-(r-b)^2}{2c^2}} \right\} \qquad (8)$$

Fig. 9 shows three typical deformation situations in the physical model and the shapes of the modified response function $F(r)$ at different vertices corresponding to the situations. Fig. 9(a) is a reference where the penetration depth is small. As shown in Fig. 9(b), when skin is being pressed with a larger d_{max}, the skin becomes more rigid, and on the contrary, the height of the response function becomes lower. However, as shown in Fig. 9(c), the swelling inside the force-applied region is ignored.

3.2. Skin deformation simulation
3.2.1. Partitioning hand surface (Fig. 2(A1))

The palmar side of a hand surface is the main contact area when objects are grasped. The basic main creases have a strong relationship with the underlying bone structure [30]. In the Digital Hand, the motions of the internal skeletal structure, such as finger bending, cause surface skin deformation, which is consistent with real joint motions of humans. Therefore, the surface anatomy by the
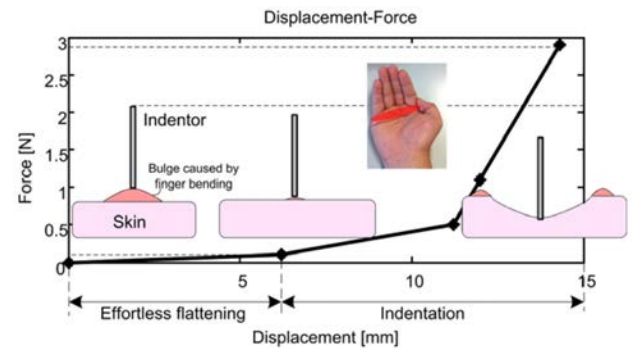

Fig. 7. Swelling bulge in different situations: (a) reference, (b) larger contact force, and (c) larger force-applied region.

Fig. 8. Indentation test to swelling bulge: bulge is very soft, only a small portion of indentation force is used to flatten the bulge.
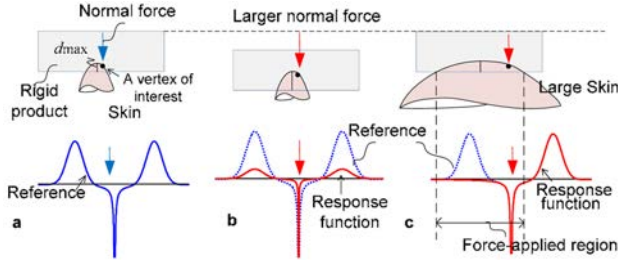
Fig. 9. Three typical deformation situations: a) reference, b) larger normal force and c) swelling within the force-applied region.

main creases was used as the partition of the palmar hand surface, as shown in Fig. 10, considering that different regions on the palm have discrepant sensitivity to externally applied surface pressure [14].

Because the partitioned sub-surfaces by main creases exhibit independence to each other during hand motions, they were treated as individual deformable sub-surfaces. The G_0 and G_{lim} of Eq.3 in each partitioned sub-surfaces also could be specified independently. Moreover, the deformation simulation involving the entire hand surface mesh was inefficient, so the partition enabled the calculation of smaller response matrices introduced in Section 3.2.2 in smaller sub-surfaces instead of calculating a large-size response matrix of a whole hand surface mesh.

3.2.2. Point-force-based discretization (Fig. 2(A2))

For a 3D triangular mesh, r in Eq. 1 should be a geodesic distance between two vertices. Therefore, a geodesic distance preserving projecting algorithm, Isometric Mapping [31] was applied, which reduced the 3D geodesic distance evaluation to the 2D Euclidean one.

In a discrete setting, the relation R_{ij} needs to be found between a force p_i acting on a vertex q_i and a displacement u_j that a vertex q_j experiences. R_{ij} can be expressed in the matrix form as Eq. 9:

$$\boldsymbol{u} = \boldsymbol{R}(d_{max})\boldsymbol{p} \qquad (9)$$

where $\boldsymbol{R}(d_{max}) = [R_{ij}(d_{max})]$: response matrix,

Fig. 10. Partition of hand surface by main creases.

$$R_{ij}(d_{max}) = G(d_{max})\frac{1}{4\pi r_{ij}} + \{-a(d_{max})\}\left\{ e^{\frac{-(r_{ij}-b)^2}{2c^2}} \right\} \qquad (10)$$

$\boldsymbol{u} = [u_1, ..., u_N]^T$ is a vector of displacements, N the number of vertices in a partitioned region, $\boldsymbol{p} = [p_1, ..., p_N]^T$ a corresponding normal force vector, r_{ij} the geodesic distance between q_i and q_j, d_{max} the maximum penetration depth among the vertices included in the active region described in Section 3.2.3.

However, in the nonlinear elasticity model of our study, G varies with d_{max}. Therefore we needed to change $\boldsymbol{R}(d_{max})$ with d_{max} in the online process. Fortunately, as Eq. 11, $\boldsymbol{R}(d_{max})$ is decomposed into a linear combination of $\boldsymbol{R}_{Bou}$ and $\boldsymbol{R}_{Gau}$, just the two component-matrices in the pre-process can be calculated, and $\boldsymbol{R}(d_{max})$ can be obtained simply by linearly combining $\boldsymbol{R}_{Bou}$ and $\boldsymbol{R}_{Gau}$ in the online process:

$$\boldsymbol{R}(d_{max}) = G(d_{max})\boldsymbol{R}_{Bou} + \{-a(d_{max})\}\boldsymbol{R}_{Gau} \qquad (11)$$

where

$\boldsymbol{R}_{Bou} = [(R_{Bou})_{ij}]$: Boussinesq response matrix,

$$(R_{Bou})_{ij} = \frac{1}{4\pi r_{ij}}$$

$\boldsymbol{R}_{Gau} = [(R_{Gau})_{ij}]$: shifted Gaussian response matrix,

$$(R_{Gau})_{ij} = e^{\frac{-(r_{ij}-b)^2}{2c^2}} \qquad (12)$$

$$a(d_{max})(R_{Gau})_{ij} = \begin{cases} 0 & (\text{if } q_i \text{ is in the force acting region}) \\ a\dfrac{G_0}{G(d_{max})}(R_{Gau})_{ij} & (\text{otherwise}) \end{cases}$$

By the decomposition of the response matrix as Eq. 11, for one Digital Hand model, all the entries of $\boldsymbol{R}_{Bou}$ and $\boldsymbol{R}_{Gau}$ can be pre-computed in each partitioned region in the pre-process, which would enable a relatively fast simulation in the following online process.

3.2.3. Detecting and enlarging collision region (Fig. 2(A3) and (A4))

Practical deformation simulations involving all the vertices lack efficiency, hence the human hand was modeled as a quasi-rigid object. *Quasi-rigid* object [21] indicates, as shown in Fig. 11, that, when the objects' surface undergoes small deformation within the vicinity of the force-applied region, called the *active region*, the remaining shape of the object still holds. When the Digital Hand comes in contact with a product surface, a *collision region* (presented by a set of vertices) can be detected. However, the collision region is not sufficient to define the active region, since the forces on these vertices can lead to displacements of vertices outside of
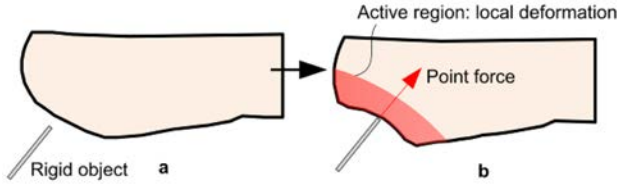
Fig. 11. *Quasi-rigid* object: (a) point force is going to be applied, and (b) after that, local deformation is formed in active area.

the collision region. To assume the required additional vertices, the fact that the modified response function has a limited effect range was considered (Section 3.1.1). Contrary to fully deformable objects where all vertices potentially experience a significant displacement, we can thus confine the active region to a local neighborhood around the collision region, which enables a faster simulation.

A collision detection algorithm [2] was adopted. The union of the collision region and its local neighboring vertices was defined as an active region. To cover the convex portion of the modified response function in Fig. 5, which corresponds to the bulges, a certain range of neighboring vertices were used as the local neighboring region for the fingers and palm. In our Digital Hand whose average distance of vertices in the Digital Hand model was about 2.5 mm, the local 5 and 7 ring neighboring vertices were used to cover the deformation range about 12.5 mm and 17.5 mm respectively, and we noticed that this range could cover the larger portion of the deformation area observed from the result of the indentation test of Fig. 6. Of course, with a larger range, better simulation results could be obtained, but involving the computation efficiency, the 5 and 7 ring neighboring vertices were regarded as a proper setting. Also, if a mesh model with a different density is used, the range of local neighboring vertices will be adjusted accordingly.

3.2.4. Separating active region (Fig. 2(A5))

If the active region partially or fully covers more than one partitioned region (Section 3.2.1), it will be separated into independent sub-active regions corresponding to each partitioned sub-surface with an independent maximum penetration depth d_{max}. The following processes of Section 3.2.5 and 3.2.6 are executed for one sub-active region.

3.2.5. Composing active response matrix with varying shear modulus (Fig. 2(A6))

Because $G(d_{max})$ varies linearly or piecewise linearly with d_{max} (Eq. 3), the value of G can be obtained at a d_{max}. Then, $\mathbf{R}(d_{max})$ was composed by linearly combining $\mathbf{R}_{Bou}$ and $\mathbf{R}_{Gau}$ that were prepared in the pre-process as Eq. 11. For one individual sub-active region, all of these entries of $\mathbf{R}(d_{max})$ were not needed, but only those related to the sub-active region. Thus, one sub-matrix $\mathbf{R}_{act}(d_{max})$

was extracted from $\mathbf{R}(d_{max})$. It only included the entries which are relevant to the vertices in the sub-active region.

3.2.6. Resolving contact using LCP (Fig. 2(A7))

The goal of this step was to realize the deformed surfaces without interpenetration. To solve to appropriate displacement distribution without interpenetration, in a sub-active region, as shown in Fig. 12(a), the contact state vector was introduced whose component s_i indicated the contact, collision or separations state at a vertex $\mathbf{q}_i$, and formulated as Eq. 13:

$$\mathbf{s} = \mathbf{R}_{act}(d_{max})\mathbf{p} + \mathbf{d} \tag{13}$$

where $\mathbf{s} = [s_1, \dots, s_M]^T$ is a state vector, M the number of vertices in a sub-active region, $\mathbf{d} = [d_1, \dots, d_M]^T$ a vector of the penetration depth at each vertex in the sub-active region: d_i is defined as the signed distance between $\mathbf{q}_i$ and its nearest triangle face on the product surface mesh, $\mathbf{p} = [p_1, \dots, p_N]^T$ a vector of the force at each vertex in the sub-active region: p_i is the normal force acting on $\mathbf{q}_i$. $s_i > 0$ indicates the *separation* state, $s_i = 0$ the *contact* state, and $s_i < 0$, the *collision* state.

The right solution of $\mathbf{s}$ and $\mathbf{p}$ must be found in order to resolve the contact which satisfied Eq. 13. This was a Quadratic Programming (QP), i.e., optimizing a quadratic function of variables, $\mathbf{s}$ and $\mathbf{p}$, subject to linear constraints on them. In Fig. 12(b), it was observed that the state s_i and the force p_i were complementary at each vertex as Eq. 14. To have a non-zero force ($p_i > 0$), there must be a zero state ($s_i = 0$, the contact state), and to have a non-zero state ($s_i > 0$, the separation state) there must be a zero force ($p_i = 0$). Therefore, the QP (Eq. 13) and the linear complementarity constraint (Eq. 14) can be combined, leading to a Linear Complementarity Problem (LCP),

$$\mathbf{s} \geq 0, \ \mathbf{p} \geq 0, \ \mathbf{s}^T\mathbf{p} = 0 \tag{14}$$

A solution of LCP can be found by the Lemke's method [32]. Once $\mathbf{p}$ is solved, according to Eq. 1, the displacements $\mathbf{u}$ can be found for all vertices in the sub-active region. By resolving the contact in different individual sub-active regions, the skin deformation of the entire active region can be realized.
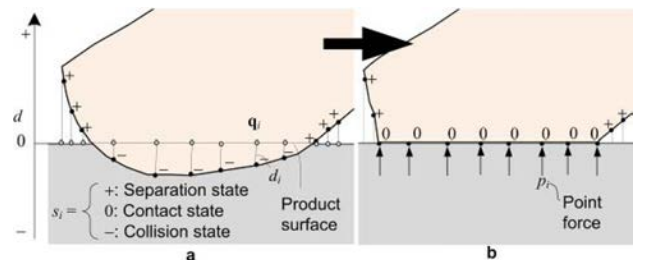

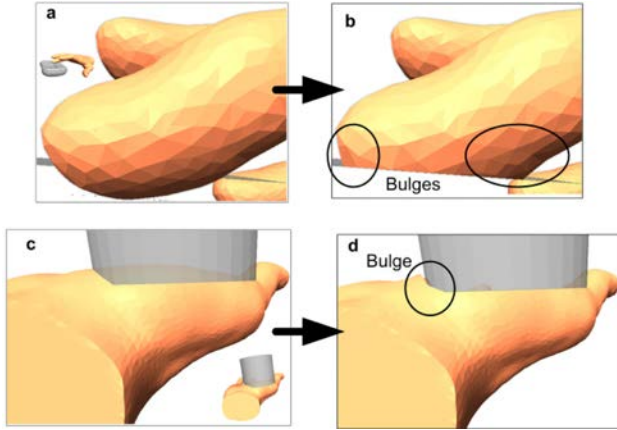**Fig. 12.** LCP: (a) initial situation, and (b) contact situation.

Fig. 13. Simulation effect of finger and palm: (a) before fingertip deformation, (b) after fingertip deformation, bulges can be observed, (c) before palm deformation, and (d) after palm deformation, a bulge can be observed.

Fig. 14. Experiment verifying finger deformation: (a) experiment setting, (b) real scene, and (c) image of contact area before and after the imaging process.

4. Simulation Results and Validation Experiment

The skin deformation simulation was tested in simple finger and palm deformation and complex deformation of a grasping hand for obtaining various contact conditions.

4.1. Simple finger and palm skin deformation

Fig. 13(a) and (c) which were captured from dynamic contact motions show the intersection between a rigid product surface and the fingertip and palm of a Digital Hand model. Fig. 13(b) and (d) illustrate the visual contact deformation after this simulation. The bulging due to the compressing-swelling effect could be observed. The time performance of the simulation is summarized in Table 3. The online processes for fingertip deformation were almost in real time, and for palm deformation, they took from 0.26 to 1.98 s depending on the maximum penetration depth.

Next, finding the setting of $G(d_{max})$ was attempted by fitting the empirical data. The experiments were conducted which recorded the contact deformation of the fingertip and the palm. The experimental settings are

Table 3. Time performance of skin deformation simulation of fingertip and palm

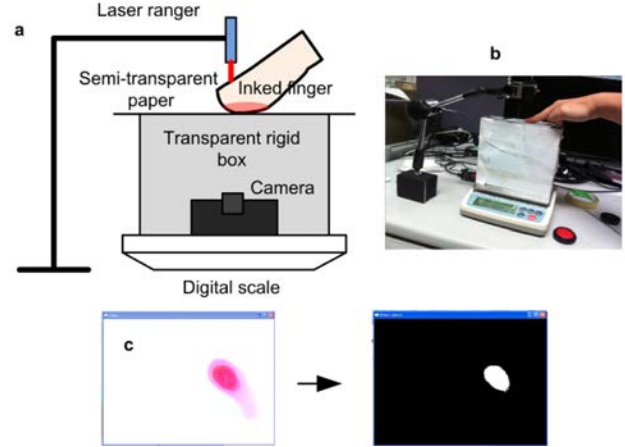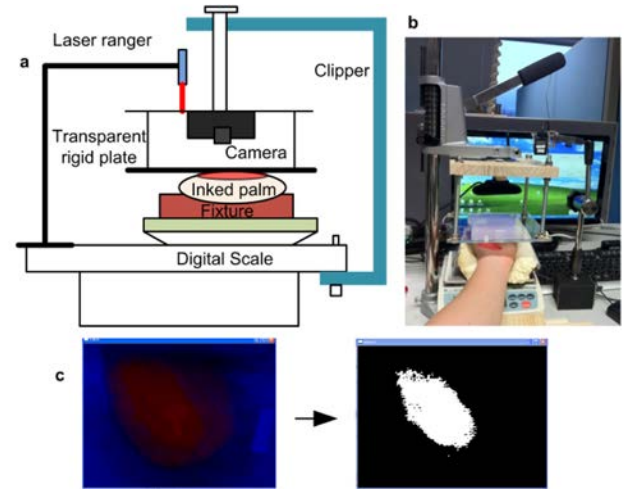|	Fingertip	Palm
Number of vertices	234	869
Number of vertices displaced in Fig. 13(a) or (c)	121	566
The maximum penetration depth	0.26-4.13 mm	0.61-6.90 mm
The maximum penetration depth in Fig. 13(a) or (c)	2.98 mm	6.1 mm
Pre-process for $\boldsymbol{R}_{Bou}$ and $\boldsymbol{R}_{Gau}$	34 s	460 s
Online process	42-82 ms	0.26-1.98 s
Hardware	Intel Core i5 1.70GHz, 4GB main memory	

Fig. 15. Experiment verifying palm deformation: (a) experiment setting, (b) real scene, and (c) image of contact area before and after the imaging process.

shown in Fig. 14, Fig. 15 and Table 4. In the fingertip measurement, the subjects were asked to press the rigid transparent plate covered by a semitransparent paper using their inked fingertip. In the palm measurement, a rigid plate covered by a semitransparent paper was pressed by the inked palms of subjects. Also, it was found that the limit penetration depth d_{lim} in Eq. 3 of the fingertip and palm was about 4 mm and 7 mm respectively.

As shown in Fig. 16, the estimated results of several fingertip and palm contact motions are compared with the measured data. Fig. 16(a) and (c) is the relation between the maximum penetration depth and the contact force (the sum of the point force at each vertex in the contact region). The results show that the estimation range (between the blue and the green curve) based on the proposed nonlinear elasticity model could effectively agree with the range of the measured contact force (the red curves) of the different subjects, which means by adjusting the values of G_0 and G_{lim}, the shape of the blue

Table 4. The setting of fingertip and palm deformation experiments

Subjects (fingertip deformation)	4 males, 23-26 years, right middle finger
Subjects (palm deformation)	5 males, 24-51 years, right hand palm
Laser ranger (Keyence IL-030)	Measuring the maximum penetration depth
Digital scale (AND EW-12Ki)	Measuring the contact force
Camera (Logitech Webcam C910)	Measuring the contact area
Computer	Image processing (OpenCV) and synchronous data acquisition
Fixture (a hard foam material)	Supporting and fixing the palm

and green curves could be controlled to best fit the experimental data (those red curves) (Section 3.1.4). On the contrary, those based on the linear elasticity model

(G was fixed at a specified value) had difficulties to fully fit the measurements. G_0 was from 5 kPa in the fingertip and 5 kPa to 50 kPa in the palm, G_{lim} was from 70 kPa to 120 kPa in the fingertip and 40 kPa to 80 kPa in the palm in the physical model.

Moreover, Fig. 16(b) and (d) shows the relation between the maximum penetration depth and contact area (the sum of the area of each triangle in the contact region). The estimations fell within the range of experimental data, and almost overlapping curves were obtained with different shear modulus, because different contact forces resulted in a relatively constant height of the swelling bulge (Section 3.1.5). For a concise expression, these overlapping curves were drawn as one.

4.2. Complex skin deformation of the grasping hand

As shown in Fig. 17, a subject (male, 27, right hand) was asked to take MRI measurements to obtain hand postures grasping a set of cylinders whose diameters were ϕ 48 mm (Fig. 17(a)), ϕ 60 mm, and ϕ 100 mm.
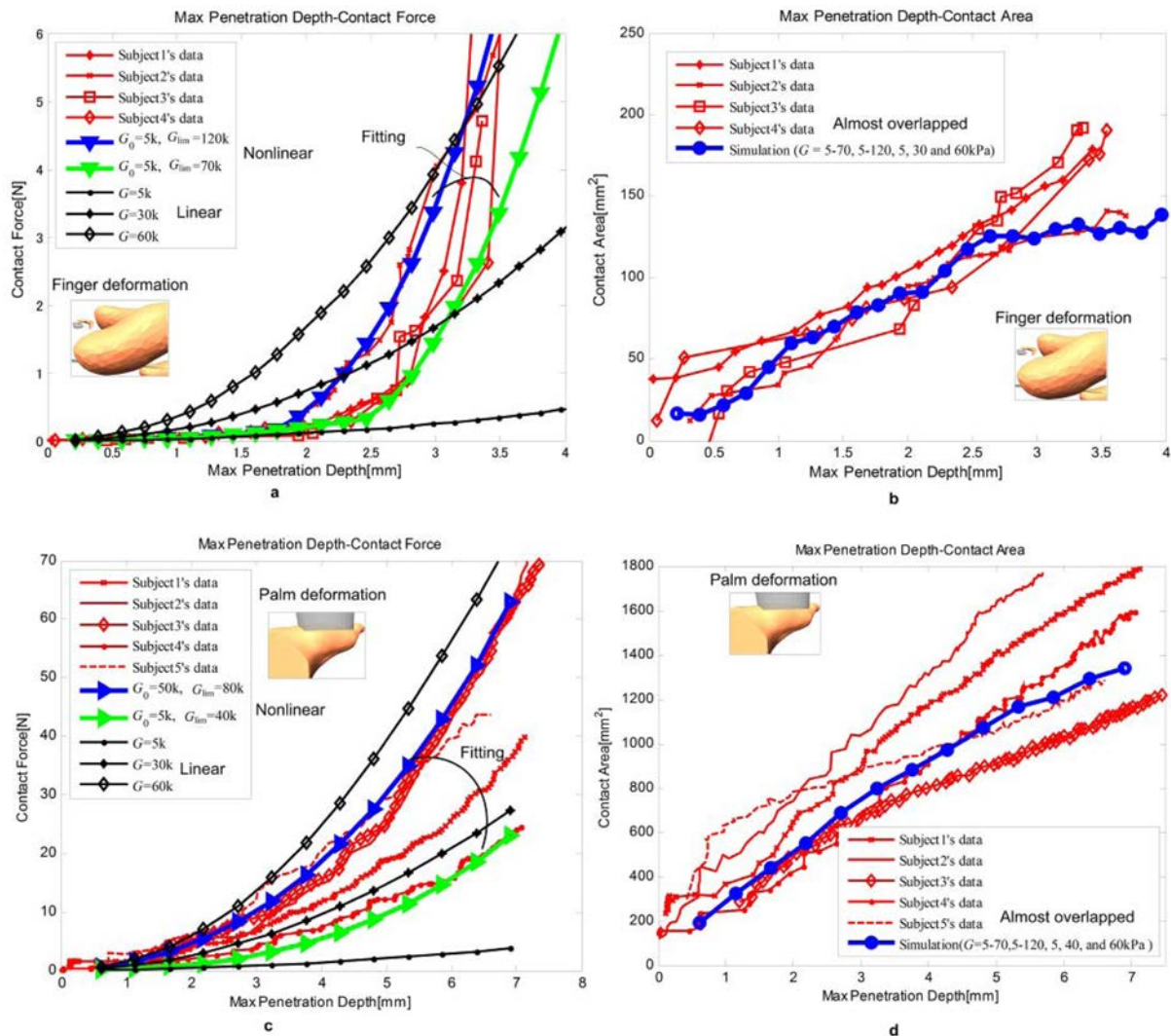

Fig. 16. Validation of deformation of finger and palm: (a) and (c) relation between maximum penetration depth and contact force (from top to bottom: finger, palm), (b) and (d) relation between maximum penetration depth and contact area (from top to bottom: finger, palm).
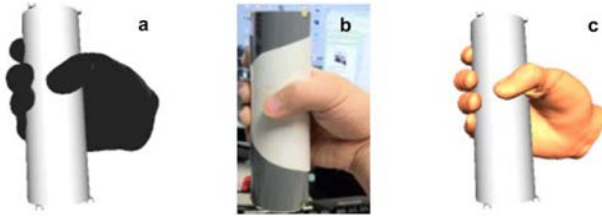
Fig. 17. Similar grasp postures gripping a cylinder of ϕ 48 mm: (a) MRI measured grasp posture, (b) real grasp posture photo, and (c) simulated grasp posture generated by Digital Hand.
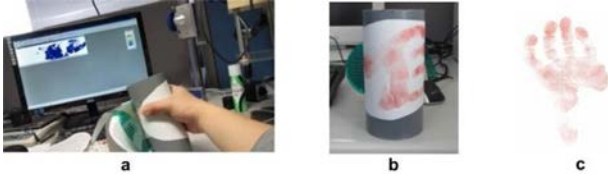

Fig. 18. Experiment validating pressure distribution of grasp posture: (a) FSCAN system, (b) Sensors mat covered by handprint, and (c) Handprint.

Next, the subject was also asked to take pressure distribution measurements (Fig. 17(b)). It was attempted to keep the two postures the same by matching them with a handprint. Fig. 18 shows the experimental setting. A sheet type of pressure sensor mat (Nitta FSCAN) with 4.2 sensors/cm^2 was wrapped around the cylinders, and then it was covered by one white paper with the same shape. The subject grasped the cylinder with an inked hand during 30 s measurements, so that the handprints could be obtained which indicated the cumulative contact area during the measurements. In contrast, a Digital Hand model of the same subject was made from the MRI measurements. By carefully manually matching the surface skin mesh and the internal bone meshes, very similar grasp postures (Fig. 17(c)) of the Digital Hand to the MRI recorded ones were reconstructed. As shown in Fig. 19(b) and (c), the other two grasps also were generated in the same way. The time performance of this simulation is described in Table 5. The online process of the deformation only needed about 20 s. The calculated $\boldsymbol{R}_{Bou}$ and $\boldsymbol{R}_{Gau}$ could be reused in different generated grasp postures of this Digital Hand model. The $G(d_{max})$ obtained in Section 4.1 was adopted for partitioned regions with slight modification of G_0 and G_{lim} for fitting empirical data in the online process.

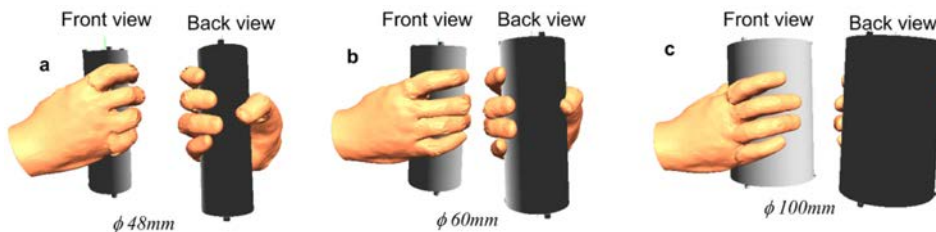   Fig. 20 shows the visual skin deformation of the hand's

Table 5. Time performance of skin deformation simulation of a grasping hand

	Grasping hand
Number of vertices	9693
Number of triangles	19382
Number of partitioned regions	19
Calculated number of component-matrices ($\boldsymbol{R}_{Bou}$ and $\boldsymbol{R}_{Gau}$)	19×2
The largest size of the matrices	869×869
Pre-process	19 minutes
Online process	About 20 s
Hardware	Intel Core i5 1.70GHz, 4GB main memory

grasp with the cylinder (ϕ 48 mm). Fig. 20(a) shows the skin without this simulation. On the contrary, Fig. 20(b) shows the results of the hand touching the cylinder. Fig. 20(c) shows the estimated pressure distribution map on palmar skin. Fig. 20(e)~(h) show the pressure map on the solid or half-transparent surface of the cylinder.

    During the 30 s measurements of grasping the three cylinders, the total contact force varied with time. It could be read from the pressure sensor mat. The ranges of the varying force were more than 100 N. The time frames of the maximum, the mean and the minimum contact force, respectively, were extracted from the recorded frame sequence. The three pressure distributions were simulated by slightly adjusting the positions of fingers in grasp postures. The maximum difference between the estimated contact forces and the measured ones is 14 N. Fig. 21 shows the comparisons between the measurements and the simulations of the maximum (Fig. 21(a)), the mean (Fig. 21(b)), and the minimum (Fig. 21(c)) contact force frames for the ϕ 48 mm cylinder grasping. The red boundaries are the contours of the handprints. The comparisons indicate that this simulation can effectively match the entire range of the contact force varying with time. Moreover, the mean force grasping posture was regarded as a natural grasp posture (Fig. 21(b)), therefore mainly the mean force grasping posture was simulated. Fig. 22 shows the same comparison of the mean frames for the ϕ 60 mm and ϕ 100 mm cylinder grasping. By referring to the handprints shown in Fig. 21 and Fig. 22, it was observed that the positions of local high pressures between the simulation and the measurement were very close to each other. Also, the highest contact pressures could be observed on both the
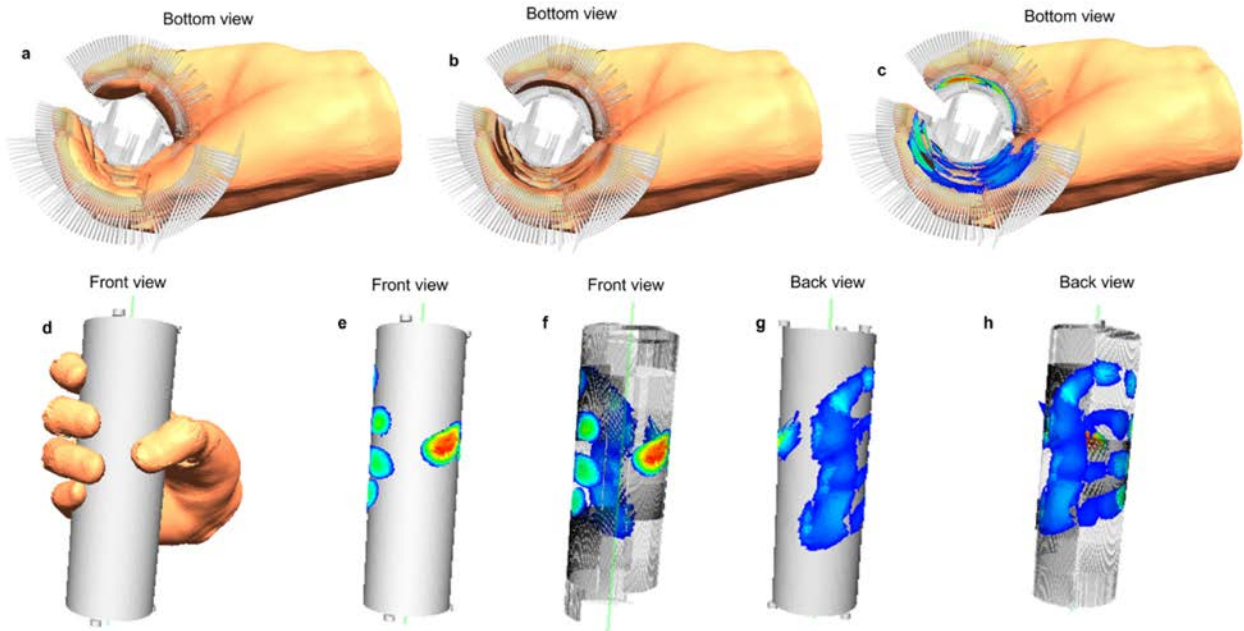

Fig. 19. Grasp posture generated by Digital Hand: (a) ϕ 48 mm cylinder, (b) ϕ 60 mm cylinder, and (c) ϕ 100 mm cylinder.

Fig. 20. Simulation of grasp posture griping a ϕ 48 mm cylinder: (a) skin before deformation, (b) skin after deformation, (c) estimated pressure distribution map, (d) grasp posture, and (e)~(h) estimated pressure distribution map.
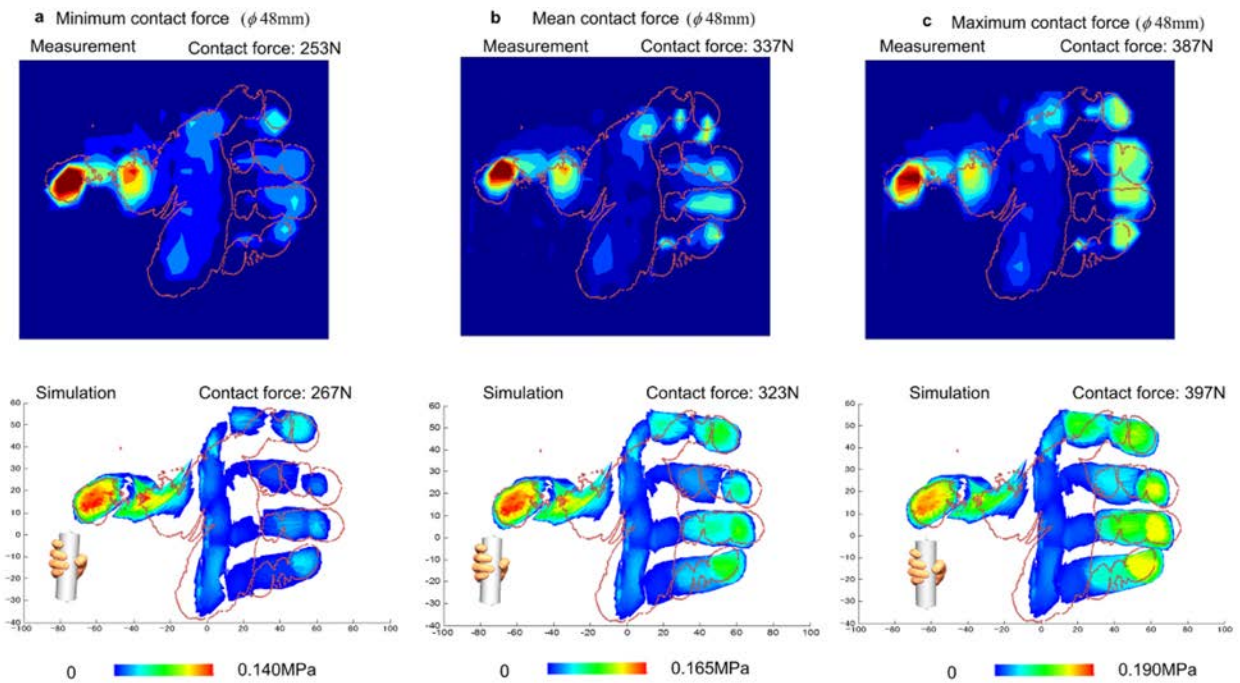

Fig. 21. Pressure distribution validation (ϕ 48 mm cylinder grasp): (a), (b) and (c) are the comparisons between measurement and simulation in the minimum, the mean and the maximum contact force.

Table 6. Comparison of pressure distribution between measurements (mean force) and simulations

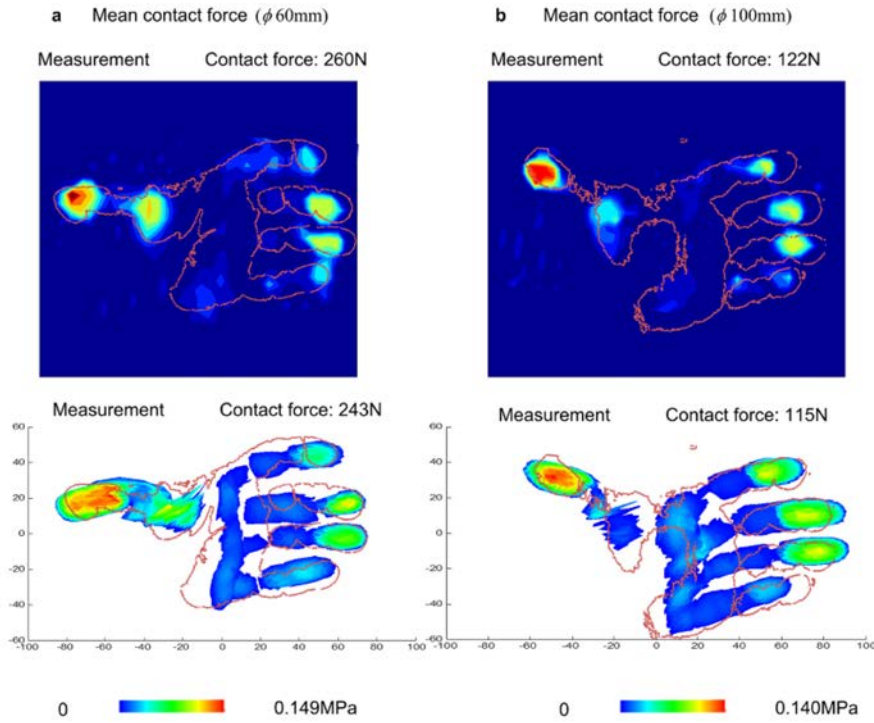| Cylinder diameter	ϕ 48 mm		ϕ 60 mm		ϕ 100 mm	
	Measurement	Simulation	Measurement	Simulation	Measurement	Simulation
Peak pressure [MPa]	0.165	0.165	0.150	0.150	0.138	0.138
Average pressure [MPa]	0.033	0.028	0.029	0.027	0.028	0.022
Total contact force [N]	337	323	260	243	122	115
Overlapped area in handprint	-	69%	-	77%	-	77%

Fig. 22. Pressure distribution validation (ϕ 60 mm and ϕ 100 mm cylinder grasps): (a) and (b) are the comparisons between measurement and simulation in the mean contact.

fingertips in the simulation and the measurement.

The quantitative comparison results for the mean contact force (Fig. 21(b) and Fig. 22) were summarized in Table 6. The estimated peak pressures, average pressures, and total contact forces were similar to the measured ones. As for the contact area, the overlapping between the simulation and the handprints accounted for 69-77%

in the handprints.

Finally, it was attempted to introduce this simulation method in an ergonomic analysis to a CAD model of the mockup of a bicycle handlebar. As shown in Fig. 23, a plausible grasp posture was manually generated and a corresponding pressure distribution was estimated on the surface of the model. It showed the possibility to in-
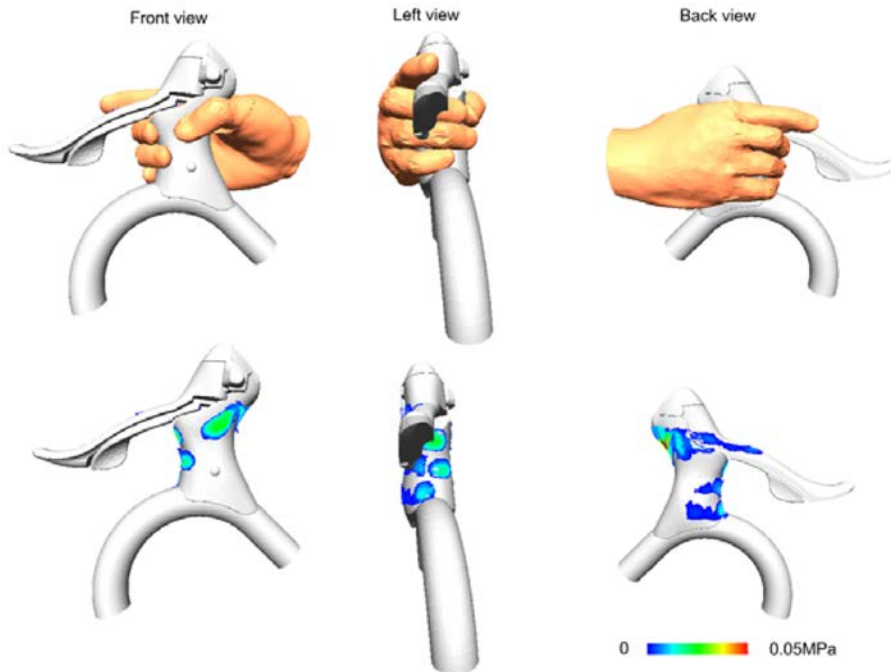

Fig. 23. The skin deformation simulation of grasping a bicycle handlebar.

corporate this simulation method in a practical virtual ergonomic assessment into the early stage of the design of handheld products. For example, a designer could use the estimated local high pressure to evaluate the comfort of an early CAD model of a product.

5. Discussion and Conclusion

In this paper, an efficient simulation method of skin contact deformation is proposed. Compared with FEM-based methods, this simulation, whose online process just needs tens of seconds for complex contact configuration, has a higher efficiency and does not burden the assessment system where there are other tasks than contact condition estimation.

The previous work [21] could effectively estimate the contact condition, but ignores some real properties of real human skin, while our proposed method realizes two important properties of human skin, the nonlinear elasticity and the compressing-swelling effect. The spatially distributed heterogeneity of the human hand is achieved by a reasonable partition by main creases on the hand surface similar to [30]. Therefore, our proposed method has enough extensibility to deal with a complex contact configuration.

The relation $G(d_{max})$, between the shear modulus and the maximum penetration in our study, is obtained by fitting experimental data. Fortunately, the range of G obtained by the experimental measurement on human hand skin [5] is within the scope of G in the physical model of our study.

A designer of the handheld product always wants to know the pressure distribution on the surface when grasping it. Hall [14] points out that local high external pressure plays an essential role in the efficiency of the work and the consumer's satisfaction. By experimental validation, the estimated pressure distributions in the simulation are closed to the real ones. Moreover, the results of the grasp simulation with different cylinders are similar to Seo's experimental conclusions [33].

Because the skin biomechanical properties of the human hand vary with the different individuals, ages, genders and nationalities, the tests on a small number of subjects are insufficient for finding the right parameter ranges of the physical model. Therefore, a database, including the parameter setting of various typical human hands, will be needed as a future work. Moreover, so far, the conditions where the contract forces act normal to the surface, i.e., the frictionless case is only considered in this paper. Further research is expected to add the friction analysis.

References

[1] G. ElKoura and K. Singh, *Handrix: animating the human hand*, in *Proceedings of the 2003 ACM SIGGRAPH/ Eurographics symposium on Computer animation*2003, Eurographics Association: San Diego, California. p. 110-119.

[2] Y. Endo, S. Kanai, T. Kishinami, N. Miyata, M. Kouchi, and M. Mochimaru, *An Application of a Digital Hand to Ergonomic Assessment of Handheld Information Appliances.* SAE Technical Paper 2006. 2006-01-2325.

[3] Y. Endo, S. Kanai, T. Kishinami, N. Miyata, M. Kouchi, and M. Mochimaru, *Virtual Ergonomic Assessment on Handheld Products based on Virtual Grasping by Digital Hand.* SAE 2007 Transactions Journal of Passenger Cars: Electronic and Electrical Systems, 2007. **116**(7): p. 877-887.

[4] Y. Endo, S. Kanai, T. Kishinami, N. Miyata, M. Kouchi, and M. Mochimaru, *Optimization-Based Grasp Posture Generation Method of Digital Hand for Virtual Ergonomic Assessment.* SAE International Journal of Passenger Cars -Electronic and Electrical Systems, 2008. **1**(1): p. 590-598.

[5] K. Dandekar, B. I. Raju, and M. A. Srinivasan, *3-D Finite-Element Models of Human and Monkey Fingertips to Investigate the Mechanics of Tactile Sense.* Journal of Biomechanical Engineering, 2003. **125**(5): p. 682-691.

[6] A. Delalleau, G. Josse, J. M. Lagarde, H. Zahouani, and J. M. Bergheau, *A nonlinear elastic behavior to identify the mechanical parameters of human skin in vivo.* Skin Research and Technology, 2008. **14**(2): p. 152-164.

[7] C. Donner, T. Weyrich, E. d'Eon, R. Ramamoorthi, and S. Rusinkiewicz, *A layered, heterogeneous reflectance model for acquiring and rendering human skin.* ACM Trans. Graph., 2008. **27**(5): p. 1-12.

[8] R. S. Johansson and K. J. Cole, *Grasp stability during manipulative actions.* Canadian Journal of Physiology and Pharmacology, 1994. **72**(5): p. 511-524.

[9] M. K. O. Burstedt, J. R. Flanagan, and R. S. Johansson, *Control of Grasp Stability in Humans Under Different Frictional Conditions During Multidigit Manipulation.* Journal of neurophysiology 1999. **82**(5): p. 2393-2405.

[10] P. Jenmalm, A. W. Goodwin, and R. S. Johansson, *Control grasp stability when humans lift objects with different surface curvatures.* Journal of Neurophysiology, 1998. **79**(4): p. 1643-1652.

[11] Y. K. Kong, D. M. Kim, K. S. Lee, and M. C. Jung, *Comparison of comfort, discomfort, and continuum ratings of force levels and hand regions during gripping exertions.* Applied Ergonomics, 2012. **43**(2): p. 283-289.

[12] L. F. M. Kuijt-Evers, T. Bosch, M. A. Huysmans, M. P. de Looze, and P. Vink, *Association between objective and subjective measurements of comfort and discomfort in hand tools.* Applied Ergonomics, 2007. **38**(5): p. 643-654.

[13] D. Welcome, S. Rakheja, R. Dong, J. Z. Wu, and A. W. Schopper, *An investigation on the relationship between grip, push and contact forces applied to a tool handle.* International Journal of Industrial Ergonomics, 2004. **34**(6): p. 507-518.

[14] C. Hall, *External pressure at the hand during object handling and work with tools.* International Journal of Industrial Ergonomics, 1997. **20**(3): p. 191-206.

[15] A. Yoxall, E. M. Rodriguez-Falcon, and J. Luxmoore, *Carpe diem, Carpe ampulla: A numerical model as an aid to the design of child-resistant closures.* Applied Ergonomics, 2013. **44**(1): p. 18-26.

[16] Y. Shimizu, K. Kawaguchi, and S. Kanai. *Constructing MRI-based 3D Precise Human Hand Models for Product Ergonomic Assessments.* in *Proceedings of 2010 Asian Conference on Design and Digital Engineering.* 2010.

Jeju, Korea.

[17] M. Ciocarlie, A. Miller, and P. Allen. *Grasp analysis using deformable fingers*. in *Intelligent Robots and Systems, 2005. IEEE/RSJ International Conference*. 2005.

[18] N. Xydas, M. Bhagavat, and I. Kao. *Study of soft-finger contact mechanics using finite elements analysis and experiments*. in *Robotics and Automation, 2000. Proceedings. ICRA '00. IEEE International Conference*. 2000.

[19] G. Q. Tao, J. Y. Li, and X. F. Jiang. *Research on virtual testing of hand pressure distribution for handle grasp*. in *Mechatronic Science, Electric Engineering and Computer (MEC), 2011 International Conference on*. 2011.

[20] W.-P. Chen, F.-T. Tang, and C.-W. Ju, *Stress distribution of the foot during mid-stance to push-off in barefoot gait: A 3-D finite element analysis*. Clinical Biomechanics, 2001. **16**(7): p. 614-620.

[21] M. Pauly, D. K. Pai, and L. J. Guibas, *Quasi-rigid objects in contact*, in *Proceedings of the 2004 ACM SIGGRAPH/Eurographics symposium on Computer animation* 2004, Eurographics Association: Grenoble, France. p. 109-119.

[22] S. Jain and C. K. Liu, *Controlling physics-based characters using soft contacts*, in *Proceedings of the 2011 SIGGRAPH Asia Conference* 2011, ACM: Hong Kong, China. p. 1-10.

[23] K. L. Johnson, *Contact Mechanics*. 1987, Cambridge, UK: Cambridge University Pres.

[24] G. A. Holzapfel, *Biomechanics of Soft Tissue*, in *The Handbook of Materials Behavior Models*, J. Lemaitre, Editor. 2001, MA: Academic: Boston. p. 1049-1063.

[25] M. A. Srinivasan, R. J. Gulati, and K. Dandekar, *In Vivo Compressibility of the Human Fingertip*. Advances in Bioengineering, 1992. **BED-22**: p. 573-576.

[26] M. H. Lu, W. Yu, Q. H. Huang, Y. P. Huang, and Y. P. Zheng, *A Hand-Held Indentation System for the Assessment of Mechanical Properties of Soft Tissues In Vivo*. Instrumentation and Measurement, IEEE Transactions on, 2009. **58**(9): p. 3079-3085.

[27] Y. Zheng and A. F. T. Mak, *Effective elastic properties for lower limb soft tissues from manual indentation experiment*. Rehabilitation Engineering, IEEE Transactions on, 1999. **7**(3): p. 257-267.

[28] J. L. Schoner, J. Lang, and H.-P. Seidel, *Measurement-Based Interactive Simulation of Viscoelastic Solids*. Computer Graphics Forum, 2004. **23**(3): p. 547-556.

[29] D. K. Pai, K. v. d. Doel, D. L. James, J. Lang, J. E. Lloyd, J. L. Richmond, and S. H. Yau, *Scanning physical interaction behavior of 3D objects*, in *Proceedings of the 28th annual conference on Computer graphics and interactive techniques* 2001, ACM. p. 87-96.

[30] T. Rhee, U. Neumann, and J. P. Lewis, *Human hand modeling from surface anatomy*, in *Proc. of the 2006 symposium on Interactive 3D graphics and games* 2006, ACM: Redwood City, California. p. 27-34.

[31] J. B. Tenenbaum, V. d. Silva, and J. C. Langford, *A Global Geometric Framework for Nonlinear Dimensionality Reduction*. Science, 2000. **290**(5500): p. 2319-2323.

[32] K. G. Murty and V. F. Yu, *Linear complementarity, linear and nonlinear programming*. 1988, Berlin: Heldermann Verlag.

[33] N. J. Seo, T. J. Armstrong, J. A. Ashton-Miller, and J. v. Baar, *Grip Forces Measured with Different Methods* 2006.

Yulai Xie is a currently pursuing his Ph.D in graduate school of information science and technology at Hokkaido University, Japan. He obtained his Master of Engineering in Measuring and Testing Technology and Instrument from Tianjin University, China in 2008. His current researching interest includes digital human modeling and digital hand modeling.

Satoshi Kanai is a full professor of systems science and informatics division in graduate school of information science and technology at Hokkaido University. He was an assistant professor in Hokkaido University from 1987-1989, and an associate professor in Tokyo Institute of Technology from 1989-1997. He is directing the projects of "Digital Ergonomics" and "Massive Digital Geometry Processing" research as a lab chair. His research interest includes Digital Prototyping, Virtual Reality and 3D Geometric Modeling. He is currently an Editor-in-chief of International Journal of CAD/CAM, and an executive scientific board of the International Journal of Interactive Design and Manufacturing. He is a member of JSPE, JSME, JSDE, IEEE and ACM.

Hiroaki Date is an associate professor of graduate school of information science and technology at Hokkaido University. He received his doctoral degree of engineering from Hokkaido University in 2003. His research interest includes point cloud data processing, geometric modelling, and finite element mesh generation.

Yulai Xie

Hiroaki Date

Satoshi Kanai